



Initial diameter effects on combustion of unsupported equi-volume *n*-heptane/iso-octane mixture droplets and the transition to cool flame behavior: Experimental observations and detailed numerical modeling

Yuhao Xu^{a,*}, Tanvir I. Farouk^b, Michael C. Hicks^c, C. Thomas Avedisian^{d,*}

^a Department of Mechanical Engineering, Prairie View A&M University, Prairie View, TX 77446, USA

^b Department of Mechanical Engineering, University of South Carolina, Columbia, SC 29208, USA

^c NASA-Glenn Research Center, Combustion and Reacting Systems Branch, 21000 Brookpark Road, Cleveland, OH 44135, USA

^d Sibley School of Mechanical and Aerospace Engineering, Cornell University, Ithaca, NY 14853, USA

ARTICLE INFO

Article history:

Received 18 November 2019

Revised 5 June 2020

Accepted 5 June 2020

Keywords:

Spray

Droplet

Droplet combustion

Low-temperature combustion

Cool flame

Primary reference fuel

ABSTRACT

This study reports an experimental and numerical investigation of droplet combustion of a miscible *n*-heptane/iso-octane mixture at a fixed mixture fraction (equi-volume) for initial diameters (D_0) in the range of $0.8 \text{ mm} \leq D_0 < 5 \text{ mm}$. This range encompasses burning transitions from hot flame (HF) combustion to the cool flame (CF) regime where radiative extinction can occur. The simulations assume spherically symmetric gas transport which was promoted in the experiments by a low gravity environment and relatively stationary droplets. Unsupported or free-floating droplets were deployed and ignited in a sealed chamber on the International Space Station to provide a low gravity condition and to accommodate the anticipated long droplet burning times (tens of seconds) for the droplet sizes investigated. The simulations incorporated multistep combustion kinetics with an embedded low temperature kinetic mechanism, non-luminous flame radiation, a model for phase equilibrium of the mixture, variable properties, unsteady gas and liquid transport, and species diffusion in the liquid. The results showed no evidence of preferential vaporization because of the close boiling points of *n*-heptane and iso-octane. For $D_0 < 3 \text{ mm}$, the mixture droplets remained in the initial HF burning regime. For larger D_0 , a transition to extinction-like behavior occurred. Measured flame radiances confirmed the importance of radiation as a controlling mechanism for driving radiative extinction and transitioning to CF burning. Radiative extinction diameters exhibited a linear relationship with D_0 which agreed very well with simulations. Mixture radiative extinction diameters were also consistent with literature values for *n*-decane, *n*-heptane, and iso-octane. Simulated droplet and flame diameters, burning rates, and flame radiances were also in good agreement with experiments.

© 2020 The Combustion Institute. Published by Elsevier Inc. All rights reserved.

1. Introduction

This study reports an experimental and numerical investigation of the burning of a binary mixture droplet comprised of *n*-heptane and iso-octane in the standard atmosphere over a wide range of initial droplet diameters (D_0), 0.8 mm to 5 mm. This range covers values where non-luminous radiative effects from the droplet flame are minimal to where they are important and lead in some cases to transitions to the cool flame (CF) burning regime.

The *n*-heptane/iso-octane system is relevant as a Primary Reference Fuel (PRF) for gasoline [1–3]. A prior study of this mixture for one particular value of initial liquid composition

showed the potential of *n*-heptane/iso-octane mixtures to transition into the CF regime [4]. A later study [5] simulated the burning of pure *n*-heptane which included luminous flame radiation via a soot model to predict transitions to CF burning and formation of a soot shell. The present work considers the burning of the *n*-heptane/iso-octane system with D_0 varying while the mixture fraction is fixed (equi-volume, PRF50) to explore transitions of burning to the CF regime and extinction. Experiments reported here were carried out on the International Space Station (ISS) to promote spherical droplet flames, to enable detailed numerical modeling (DNM) to predict the influence of D_0 on droplet burning for a fixed initial droplet composition, and to provide the long duration experimental times needed to observe the complete burning history of the large droplets examined.

* Corresponding authors.

E-mail addresses: yuxu@pvamu.edu (Y. Xu), cta2@cornell.edu (C.T. Avedisian).

Table 1
Selected properties of *n*-heptane and iso-octane.

Property	<i>n</i> -heptane	iso-octane
Formula	C ₇ H ₁₆	C ₈ H ₁₈
Stoichiometric coefficient ν	11.0	12.5
Molecular Weight (g/mole) [17]	100	114
Boiling point T _b (K) [17]	372	372
Flash point (K) [17]	269	261
Liquid density ρ_L (@298 K, kg/m ³) [17]	680	692
Liquid density ρ_L (@T _b , kg/m ³) [18]	608	638
Heat of vaporization (@T _b , kJ/mol) [17]	31.8	30.8
Lower heating value (MJ/kg) [19]	44.6	44.3

It is important to note that the D_o values considered here are not representative of droplets in fuel injection processes in combustion engines, where D_o is often well under 100 μm . Instead, the motivation for examining droplet sizes nominally an order of magnitude larger is to facilitate accessing experimentally certain physics of the burning process that would be more difficult for small droplets. These include radiation, unsteady gas and liquid effects, detailed combustion chemistry, preferential vaporization, and multicomponent diffusion of mixture components inside the droplet.

The influence of D_o on burning under conditions where external convective effects are minimal has long been known to affect the physico/chemical processes of burning noted above [6–15]–[16]. Most of the prior work concerned single component systems. Regarding mixtures, the study of *n*-heptane/*n*-hexadecane mixture droplets considered the influence of D_o for a fixed mixture fraction [15]. No comparisons with experiments were reported for this mixture.

The present work includes DNM and compares predictions with the extensive database for the *n*-heptane/iso-octane system. This mixture is relatively simple because of the similarity of its properties, as summarized in Table 1. The potential for the burning process to be terminated by a micro-explosive event is thereby eliminated because of the close boiling points, which will facilitate interpreting the experimental results.

The composition of the *n*-heptane/iso-octane system examined is equi-volume to compare with limited prior work [4] that studied this composition but for only one large initial droplet diameter (3.51 mm). The equi-volume composition is not necessarily indicative of octane numbers characteristic of gasoline. Nonetheless, the equi-volume mixture examined here over a range of D_o provides a link to [4] for comparing with transitions to CF combustion.

Because numerical modeling is an important part of the present study, we chose an experimental configuration that is conducive to DNM. In particular, gas transport around a burning droplet that is driven entirely by the fuel evaporation process without any external flow effects leads to a one-dimensional (1-D) transport that facilitates numerical modeling. The resulting burning configuration is spherically symmetric. If soot aggregates form, they will be positioned between the droplet and flame in a sort of porous shell-like structure by a balance of forces acting on them: inwardly directed thermophoresis and outwardly directed flow from the evaporating fuel. This multiphase configuration still links to a spray that sets the initial conditions for combustion in engines [20], where the in-cylinder environment can include the presence of fuel droplets [21–24].

The range of D_o examined here is sufficiently large that a transition from hot flame (HF) diffusive extinction to radiative extinction and potentially CF burning is anticipated based on the simulations reported in [4]. The burn time of droplets at the upper end of this range can be several tens of seconds so that their combustion dynamics can only be investigated in the ISS environment [25].

Table 2
Conditions examined for 50/50 *n*-heptane/iso-octane droplets.

Operations no.	D_o (mm)	Ignition energy (J)
GB [18]	0.52	0.1 [18]
ISS E169M09	0.80	12.05
ISS E211M09	1.24	6.424
ISS E178M09	1.86	12.05
ISS E216M03	2.28	6.424
ISS E169M03	2.65	12.05
ISS E211M02	3.15	6.424
ISS E216M02	3.44	6.424
ISS E211M03	3.77	6.424
ISS E211M04	4.27	6.424
ISS E211M06	4.80	6.424

The data discussed in this paper are compared to a DNM that incorporates detailed combustion kinetics, one-dimensional evaporation, spectral radiative interactions, and variable thermal and transport properties that depend on temperature and concentration. The next sections outline the experimental design and procedures, data analysis, and the DNM followed by a presentation of results.

2. Description of the experiment

2.1. Experimental design

Spherically symmetric gas transport and a 1-D flow process are promoted by carrying out experiments in a low gravity environment so that the resulting data can be modeled. The large D_o where transitions to CF burning in the standard atmosphere are expected required experimental times on the order of tens of seconds to observe their complete burning history. This was accomplished by using the facilities of the ISS.

Relatively stationary droplets were deployed into a stagnant ambient and burned in the low gravitational field of the orbiting ISS so that the influence of buoyancy and forced convection (as manifested by appropriately defined Rayleigh and Reynolds numbers) were significantly reduced. The procedure for creating free or unsupported droplets involved first forming a liquid bridge across two needles, stretching the needles slightly, then rapidly withdrawing them to create ostensibly a stationary free-floating droplet in the low gravity environment. Concurrently, Kanthal coils positioned on opposite sides of the droplet were energized to ignite the droplets, and the wires were then rapidly retracted to provide an unobstructed field for the burning process. Video cameras recorded the complete droplet burning history. Further details of the experimental hardware and procedures are given in [9,25–27]. A summary of the conditions for droplet ignition is given in Table 2. Included are the ignition energy imparted by the Kanthal coils, the initial droplet diameter, and the operation number of the experiment.

The primary diagnostic of the experiments was video imaging of the burning process. It provided the raw ‘data’ from which quantitative information about the droplet combustion physics was obtained. The droplet burning process was recorded by a High Bit-Depth Multispectral (HiBMs) camera (1 MP at 30 fps) with a backlight source and by a color camera (0.3 MP at 30 fps).

For all experiments reported here, the radiant field surrounding a burning droplet was recorded by narrowband and wideband radiometers. The narrowband radiometer had a transmission cut-off at 7.145 μm and a full width at half maximum (FWHM) of 1.54 μm , and the wideband radiometer covered wavelengths between 0.1 μm and 54 μm . These settings were employed so that

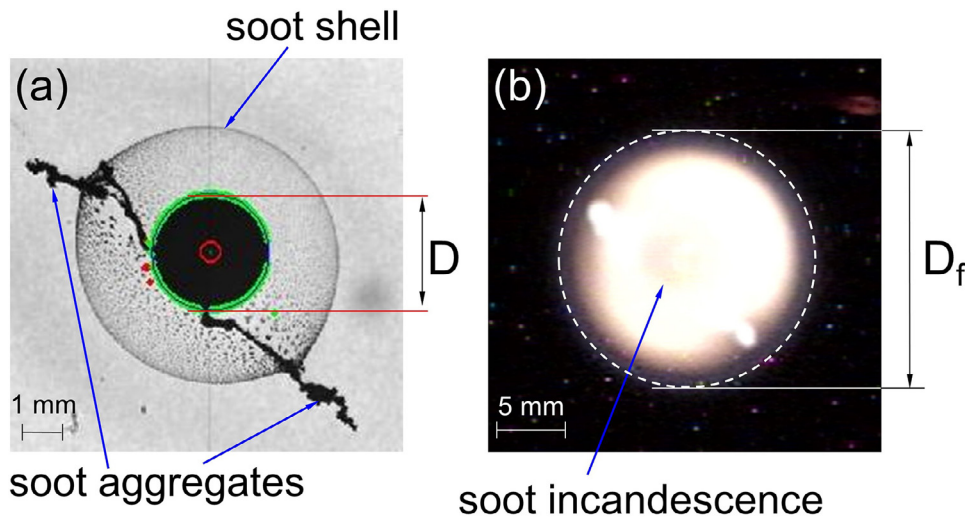


Fig. 1. Exemplar images illustrating the image analysis processes of ISS droplets for (a) droplet diameter D and (b) flame diameter D_f . Note different scales. (For interpretation of the references to color in this figure, the reader is referred to the web version of this article.)

the narrowband and wideband radiometers were optimized for sensitivity to the CF and HF, respectively.

The narrowband radiometer was designed to detect emissions from the peak water band at $6.3 \mu\text{m}$. This radiometer is a thin film-based thermopile from Dexter Research (Model 2 M - Dexter custom P/N DX-0918) and is filtered with a combination of a silicon Long Wave Pass (LWP) filter with a cut-on wavelength of $5.0 \mu\text{m}$ and a sapphire window that cuts off at $\sim 7.0 \mu\text{m}$. The filter effectively isolates the desired spectral region of interest, i.e., the detection of water emission. Since these radiometers are sensitive to the temperature of the environment in which they operate, this was considered when calibration was performed and when the radiometer was mounted to the structure. Calibration was performed at ambient temperatures (ca. 23°C), and mounting of the radiometers to the chamber structure was such that the calibration temperature was maintained throughout testing. The gain of the narrowband radiometer was set so that signal saturation did not occur below an irradiance of 3.0 mW/cm^2 .

The process of droplet deployment, ignition, and recording of the burning process was performed in an entirely computer-controlled arrangement. Wireless links were established from the orbiting ISS to NASA-Glenn Research Center (Cleveland, O.H.) and then Cornell University (Ithaca, N.Y.) to allow real-time adjustments to the initial conditions of the experiments. The onboard assistance of astronauts was not required during the experiments.

2.2. Analysis of video images

Important to the ability to obtain quantitative information about combustion physics from digital video images are software tools to extract physical dimensions from individual video frames. For the study reported here, data were extracted from individual video frames by an automated algorithm [28] or a manual process using a commercial software package (Image-Pro-Plus v6.3), with the latter being needed for measurements of the flame diameters.

Figure 1 shows a black-and-white (BW) image that illustrates the droplet boundary (outlined by the green circle in 'a') identified by the automated algorithm to obtain an area-averaged droplet diameter. The soot shell is clearly visible in Fig. 1a, while Fig. 1b shows the flame image. Noticeable in Fig. 1a are soot 'tails'. These are created by the retraction process of the needles that initially suspend a liquid bridge. The retraction creates an initial

gas flow that stretches laterally the sooting pattern (which is a good marker for gas flows) that is apparent in Fig. 1a.

For the flame diameter D_f , a manual approach involved positioning a virtual ellipse around the flame boundary (cf, the dotted lines in Fig. 1b), which was defined as the outer edge of the blue luminous zone. Equivalent diameters using this method were then obtained as $(H \times W)^{0.5}$, where H and W are major and minor axes of the ellipse, respectively. These methods of image analyses and data reduction are consistent with those adopted previously [9,29] for similar images from ISS experiments. The photographs in Fig. 1 are among the best obtained for this mixture to illustrate the structure of the sooting field. Figure 1a shows a virtual ellipse surrounding the droplet from the automated method. Figure 1b shows a manually positioned virtual ellipse around the flame. The incandescence of soot creates the bright yellow core shown in Fig. 1b.

The uncertainty of data reduction operations from video images arises from identifying the boundary thickness of the droplet and flame, which consists of about 3 and 5 pixels, respectively. The diameter of the largest droplet measured in this study is around 4.82 mm (163 pixels) and thus has a corresponding uncertainty of $\pm 1.8\%$. The smallest droplet size reported here is about 0.59 mm (20 pixels). The measurement uncertainty for such a small droplet is at $\pm 15\%$, though very few measurements are performed for such small droplets in the present work. Note that measurements can be made to this precision, but droplets cannot be generated with this same precision. For flame diameters, the smallest flame diameter is approximately 7.57 mm (52 pixels) with an uncertainty of $\pm 9.6\%$, and the largest flame diameter is about 30.14 mm (207 pixels) with a measurement uncertainty of $\pm 2.4\%$.

3. Numerical modeling

The detailed numerical model used in this paper was described previously [30–33]. New to the simulation is a different kinetic mechanism and thermal/physical property database for the PRF mixture. The detailed and comprehensive kinetic mechanism employed in the computations for *n*-heptane and iso-octane included low, intermediate, and high temperature kinetic regimes. The resulting kinetic model was sufficient to resolve hot ignition, high temperature kinetics, and Low Temperature Combustion (LTC) behaviors.

The mechanism consisted of 298 species, 1916 reactions, and associated chemical thermodynamic properties. It was reduced

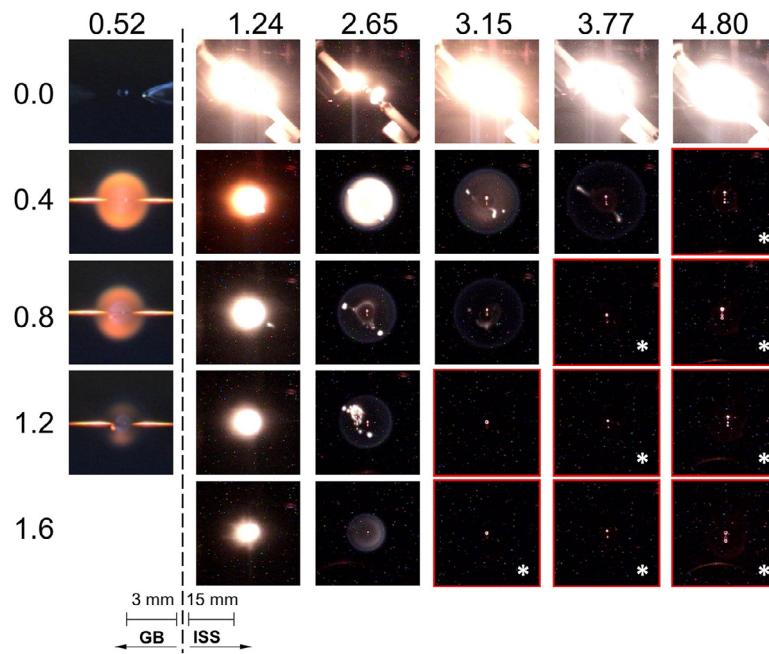


Fig. 2. Selected color images from GB and ISS 50/50 *n*-heptane/iso-octane experiments. Images for $D_o = 0.52$ mm are from [18] for comparison. Note differences in scale. Numbers on top indicate D_o (mm) and vertically are normalized time t/D_o^2 (s/mm^2). Images with a red frame are those after HF extinction where the flame is not visible (e.g., For $D_o = 3.15$ mm, the flame is not visible after $t/D_o^2 = 0.8$ s/mm^2). The asterisks identify photographs where the burning is in the CF regime with the burn rate still much higher than pure evaporation. The GB photos are from [18] and show a droplet supported by two $14 \mu m$ SiC fibers (unlike the ISS droplets which are unsupported). (For interpretation of the references to color in this figure legend, the reader is referred to the web version of this article.)

from an *n*-heptane kinetic model [31] that included an embedded iso-octane subset [34] and PAH sub-model components [35] to consider the potential for the formation of high molecular weight species that could lead to soot formation. The formation of soot aggregates and the soot shell was not specifically included in the model, though the kinetics included the formation of soot precursor species.

A phase equilibrium model for binary fuel evaporation and a species diffusion equation in the liquid were incorporated. The DNM assumes a 1-D gas transport without liquid dissolution interactions involving gas phase combustion intermediates such as those that could be important for high pressure droplet burning. The DNM can accommodate a kinetic mechanism of any size limited only by computational power. The simulation solves the conservation equations of energy and mass for the liquid and gas phases along with the equations of species diffusion in the droplet and surrounding gas for both the gas and liquid phases. Multi-component diffusion is taken into account in the gas phase species equation.

Radiative effects are accounted for via a spectrally resolved statistical narrowband radiation model. Additionally, the *n*-heptane/iso-octane non-polar mixture was assumed to be ideal, and Raoult's law was applied. The properties of the liquids were taken from [36].

The present study does not incorporate a model for soot formation. The soot shell cannot, therefore, directly be predicted except indirectly by assuming that it will reside where the concentration of soot precursor species is highest (e.g., acetylene [37]). Recent work [38] showed that simulations neglecting soot for the comparatively mildly sooting *n*-heptane gave reasonably good agreement with experiments for small droplets ($D_o < 0.6$ mm), and we anticipate the same for iso-octane. A later study incorporated a soot model in an analysis of pure *n*-heptane droplet combustion [5]. In the present study which concerns a binary miscible mixture, the decision not to incorporate a soot model was a consideration of

the lightly sooting components at the expense of a detailed kinetic mechanism and computational costs involved.

Symmetry conditions are imposed at the center of the droplet. At the liquid/gas interface, the continuity of fluxes of energy and species are considered. The far-field boundary (~ 200 times the initial droplet diameter) is defined using a Dirichlet boundary condition by prescribing ambient composition and temperature (i.e. X_{O_2}/X_{N_2} 0.21/0.79 and 298 K). A trapezoidal high temperature region is used as an initial condition representing the hot wire ignition source. It was clearly shown in [38] that higher ignition energy can wash out a significant portion of the initial transient period of burning. Therefore, as D_o was changed, the ignition energy provided in the domain was adjusted, noting that larger droplets required higher ignition energies. This adjustment was made in such a way that the energy deposited to the droplet remained more or less constant. The ignition energy was varied by keeping the ratio of the volume of the droplet to the volume of the initial ignition energy region constant for all the different droplet diameters considered in this study.

The computational grid consisted of 50 and 250 points in the liquid and gas phases, respectively. Adjustment of combustion kinetics, or thermophysical properties to reduce differences between simulated and experimental was not performed.

4. Results and discussions

Figure 2 shows selected color images for burning 50/50 *n*-heptane/iso-octane droplets. Also shown in the first column is a 0.52 mm diameter droplet for comparison from a GB experiment [18]. The flame luminosity is clearly strongly affected by D_o . The luminosity decreases with increasing D_o , and the flame eventually disappears for large D_o . These effects can be explained from measurements and predictions of flame radiance and flame temperature.

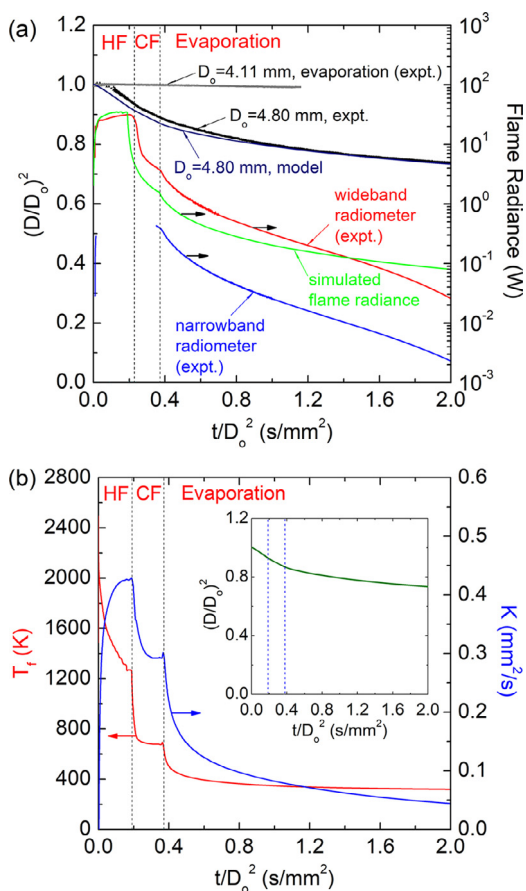


Fig. 3. (a) Evolution of droplet diameter and flame radiance for 50/50 *n*-heptane/iso-octane ($D_0 = 4.80$ mm); (b) simulated flame temperature, burning rate, and evolution of droplet diameter (inset) for $D_0 = 4.80$ mm.

Figure 3 shows such data for one particular value of D_0 to illustrate. Taking the flame luminosity (brightness) as a qualitative measure of soot formation [39], the photographs in Fig. 2 indicate that soot formation alternately increases then decreases during burning. As burning progresses, radiant heat from the flame increases in the HF regime. Figure 3a shows a simulation of the evolution of flame radiance for $D_0 = 4.80$ mm. The flame brightness also increases as shown in Fig. 2. The flame brightness eventually decreases as burning progresses. The flame temperature also decreases in this period as shown in Fig. 3b and eventually reaches a soot inception temperature threshold [40] where no soot forms, but the droplet is still burning. A blue sootless flame then results, as seen in Fig. 2 (cf. 2.65 mm:0.8 s/mm²).

The flame luminosity decreases as flame temperature decreases, and a point is reached where the flame is not visible in the experiments. The (predicted) gas temperature in this regime is still well above ambient, as shown in Fig. 3b. This is the period of CF burning for the mixture. The photographs marked by an asterisk in Fig. 2 correspond to conditions where burning is believed to be in the CF regime, and the flame is not visible. With decreasing luminosity for large droplets, a radiative extinction phenomenon is generally observed [41], which is consistent with the present study for $D_0 > 3$ mm as shown in Fig. 2. By fixing the mixture fraction as done here, the trends noted above are due entirely to changes in D_0 . These trends are qualitatively consistent with prior work for single-component fuels. For the *n*-heptane/iso-octane system, the iso-octane concentration has been shown [4] to have an important effect on transitions to CF burning.

Figure 4 shows selected BW images of droplets that illustrate the sooting dynamics for 50/50 *n*-heptane/iso-octane droplets for several values of D_0 (note different scales for the GB and ISS experiments).¹ For small droplets ($D_0 < 2$ mm), the soot shell is intact throughout the combustion process, and the flames have a bright yellow core (Fig. 2) due to the incandescence of the soot aggregates inside the flame. With increasing D_0 , the soot shell appears to grow thinner (Fig. 4) and less dense, which is consistent with diminished flame luminosity as the droplet size increases. This effect is due to increased radiation losses from the droplet flame to the ambient and the decreased flame temperature as D_0 increases.

Time zero in Figs. 2 and 4 is assigned to the BW video frame prior to the frame in which the soot cloud or particles first appear around the droplet. The retraction movement of the hot-wire igniter is then used to time synchronize the BW and color image data. The movement or retraction of the hot-wire igniter is not used to define time zero because for experiments performed in this study, the igniter starts to retract about 0.4 s (12 images frames) on average after the visible flame is observed.

Quantitative measurements of the evolution of droplet diameter for 50/50 *n*-heptane/iso-octane experiments are shown in Fig. 5 in scaled coordinates for the indicated values of initial droplet diameter.² Also shown is a portion of the evolution of diameter for a non-burning PRF50 droplet ('evaporation' in Fig. 5) for comparison. The results of the DNM simulations are shown by the solid lines.

The small differences between experiments and predictions are possibly a result of early transients and the initial conditions used, such as ignition energy, to simulate the experiments. Note that slightly different ignition energies were used for different droplet sizes during experiments since some of the droplets were not ignited when igniter settings remained unchanged as D_0 varied (e.g., the 4.11 mm test run shown in Fig. 5). It was previously reported that the initial ignition energy can significantly affect the transient establishment of the hot flame burning regime [38]. Therefore, different ignition energies in experiments and simulations may be responsible for the small differences shown in Fig. 5.

The trends in Fig. 5 do not provide evidence of any obvious preferential vaporization effect in the hot flame (pre-extinction) region as, for example, where vaporization would occur in the order of the component volatilities. One component would evaporate first and be depleted from the droplet, followed by the second. The burn rates would then correspond to the component that is dominating vaporization. For *n*-heptane and iso-octane, the key properties that would control this effect - boiling point and heat of vaporization - are very close, as shown in Table 1. On that basis, even if one component were to control vaporization first, there would be a seamless transition to the second component, and the burn rates would be the same. The evolution of droplet diameter could not reveal such a transition which does seem to be the case with the data shown in Fig. 5. The noticeable decrease in burn rate for the larger droplets is attributed to radiative losses that reduce the flame temperature and lead to a transition of burning to the CF regime. The reduction in flame temperature is supported by simulations, for example, in Fig. 3 which shows a significant reduction of predicted flame temperature in the CF regime.

For $D_0 < 3$ mm, the evolution of the scaled droplet diameter in Fig. 5 is nearly linear, with droplet flames being visible throughout the burn history as shown in Fig. 2. This is the HF regime. In a second period illustrated by $D_0 = 3.77$ mm, the mixture burn rates

¹ The photographs in Fig. 4 show a stain on the quartz window of the combustion chamber, which could not be replaced during operation of the ISS experiments reported here. The stain had no effect on burning or on the computer processing of the video images to extract quantitative data.

² All of the data plotted in the paper are provided in Excel files in the Supplementary Materials Section.

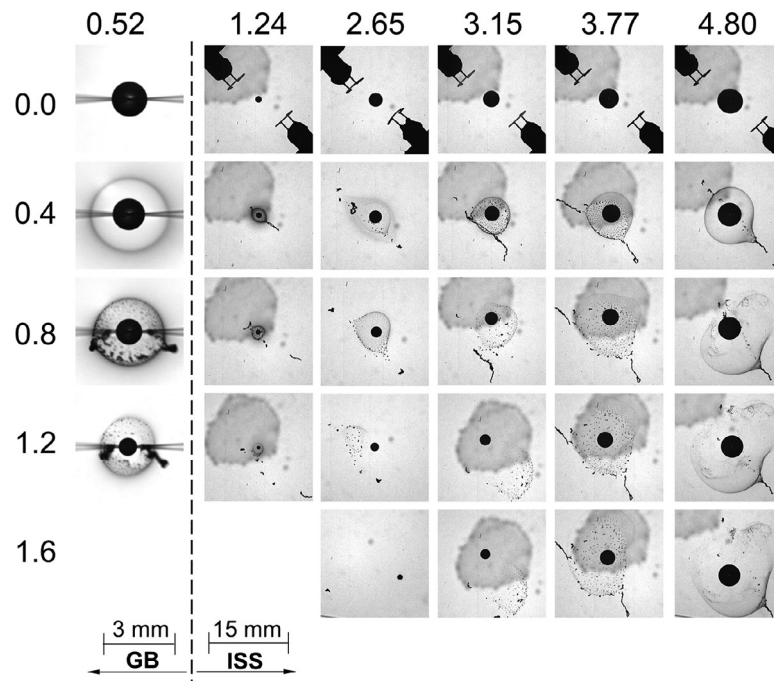


Fig. 4. Selected BW images from GB and ISS 50/50 *n*-heptane/iso-octane experiments. Images for $D_o = 0.52$ mm are from [18] for comparison. Note differences in scale. Numbers on top indicate D_o (mm) and vertically represent normalized time t/D_o^2 (s/mm²). The dark patch is a stain on the viewing port. The GB photos are from [18] and show a droplet supported by two 14 μ m SiC fibers (unlike the ISS droplets).

are significantly reduced, and a flame is not visible. A useful comparison in this late period of burning is with a non-burning, evaporating droplet for the 50/50 mixture. If burn rates were higher than for pure evaporation, this would be evidence for a warmer ambient and the possible presence of a flame even though it is not visible. Using $D_o = 4.11$ mm evaporation data shown in Fig. 5 as representative, the trends show that the mixture burning rate is higher than for pure evaporation. On this basis, we can conclude that a flame may still exist in the CF regime even though it is not visible.

Figure 3a shows more detailed information that is suggestive of a transition from HF burning to a CF regime for the particular case of a $D_o = 4.80$ mm droplet. Experimental measurements (black symbols) and numerical predictions (navy solid line) show good agreement. Also included in Fig. 3a are measurements from radiometers that were positioned around the droplet flame in the combustion chamber to record both narrowband and wideband emissions. The radiometer data provide insights into what cannot be discerned from the color video images. Predicted and measured flame radiances are in good agreement. Figure 3b shows computed flame temperatures and burn rates in the HF and CF regimes.

Early in the burning period, the flame is bright and visible, narrowband emission data are saturated, and wideband data are nearly constant up to a scaled time of about 0.234 s/mm². Thereafter, wideband emissions drop, and the flame is no longer visible. Yet, the evaporation rate is significantly higher than for pure evaporation (with the $D_o = 4.11$ mm PRF50 case used for comparison, as noted previously). We take this as evidence of transitioning to CF burning with the radiative ‘extinction’ diameter being about 4.64 mm. During this period, the flame further cools until at 0.371 s/mm²; the rate of change of the wideband emissions abruptly decreases, and CF burning ends. Subsequently, the droplet is simply evaporating in the surrounding hot gases while the heat diffuses to the surrounding. Ultimately, the regression rate of the droplet diameter approaches the pure evaporation limit in the standard ambient. The trend of the simulated flame radiance

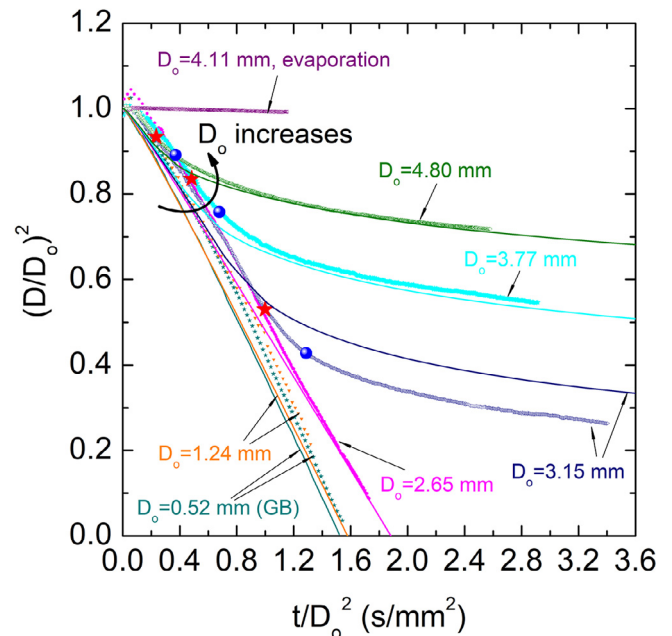


Fig. 5. Evolution of droplet diameter for 50/50 *n*-heptane/iso-octane droplets for the indicated D_o . Symbols and lines represent experimental measurements and numerical predictions, respectively. The measured and predicted data for $D_o = 0.52$ mm are from [18] and [4], respectively, and included for comparison. For data with $D_o > 3$ mm, red stars signify the end of HF burning, and the blue circles signify the end of the CF regime. The data are provided in the Supplementary Materials Section. (For interpretation of the references to color in this figure legend, the reader is referred to the web version of this article.)

shown in Fig. 3a is in agreement with experimentally measured radiance.

Figure 3b shows predicted flame temperatures and instantaneous burning rates for $D_o = 4.80$ mm. The simulated flame

temperature is about 700 K in the CF period compared to about 2000 K in the early HF period, which confirms the presence of the CF burning mode. The predicted peak temperature profile also shows a sharp transition after the CF mode ends, and the droplet continues to undergo evaporation driven only by the residual hot product gases. The predicted burning rate evolution shows a distinct, two-stage burning behavior. In the HF burn regime, the burning rate is found to continuously increase until the maximum radiant emission is attained, after which the burn rate decreases significantly. The burning rate evolution confirms that the CF burning mode takes place only for a very short duration.

Similar to prior predictions [4] during high temperature burning, the major combustion products are predicted to be CO_2 and H_2O . The transition to low temperature burning coincides with a significant decrease in the rate of production of CO_2 and an accompanying accumulation for its precursor species, CO . The inhibitive nature of iso-octane to the low temperature kinetic behavior of pure *n*-heptane suppresses the second stage burn time associated with CF droplet burning. Despite the short duration of the CF burn, the second stage burn shows all the distinct characteristics of low temperature kinetics; higher concentrations of H_2O_2 , CH_2O , CH_3CHO , and ketohydroperoxides ($\text{C}_7\text{H}_{14}\text{O}_3$) (not shown here). A flux analysis indicates that the bulk of *n*-heptane consumption during CF droplet burning occurs through H abstraction reactions by OH radicals and, to a much lesser extent, by HO_2 radicals. Beta scission reactions of the resulting *n*-heptyl radicals typically dominant in HF cease to be significant, and are instead consumed by addition reactions with O_2 to form RO_2 radicals. Alkyl peroxy radical isomerization follows, forming QOOH. The QOOH formed is consumed through two competing pathways: formation of QOOH O_2 through O_2 addition; and decomposition to alkenes, carbonyl, QO, OH, and HO_2 .

During the second stage combustion of the droplet, a major portion of the QOOH undergoes cyclization of the diradical to form cyclic ethers (QO). The decomposition of QOOH results only in radical propagation. QOOH O_2 surviving the decomposition reaction participates in the isomerization processes to form $\text{C}_7\text{H}_{14}\text{O}_3$. As for the iso-octane, it undergoes H abstraction predominantly by OH radical and also by H and HO_2 radical forming the iso-octyl radical. The iso-octyl decomposes to produce iso-butene (C_4H_8), propene (C_3H_6), and some C_7 alkenes. As CF droplet burning extinguishes, the droplet is still composed of ample quantities of both *n*-heptane and iso-octane.

Figure 6 shows the influence of D_0 on the radiative extinction diameter for the mixture, D_{ext} . Also shown are data of HF extinction diameters from Ref. [42] for pure *n*-heptane and *n*-decane and Ref. [29] for pure iso-octane burning with air at 1 atm. The agreement of the measured and simulated HF extinction data for the PRF50 mixture is excellent. The trends show a linear variation of D_{ext} with D_0 .

The comparisons of the mixture and single-component radiative extinction data in Fig. 6 show an interesting coincidence. The high temperature kinetics for *n*-heptane, *n*-decane, and the PRF mixture will not vary much as they are mostly beta scission and H-abstraction reactions. To some extent, there is some thermal decomposition/pyrolysis, but that is in the extreme fuel rich side. The radiative extinction of large alkanes is driven by a balance of the heat of combustion and heat loss from the flames. *n*-Decane has a higher heat of combustion, specific heat, and heat of vaporization – so *n*-decane will need higher heat feedback from the flame to the droplet. As a result, *n*-heptane and *n*-decane will then show similar hot flame extinction characteristics, which is consistent with the results in Fig. 6. It is worth noting that it was previously shown [31,42] that pure hydrocarbons have a linear relationship of D_{ext} with D_0 in the HF burning regime. This same linear trend is shown

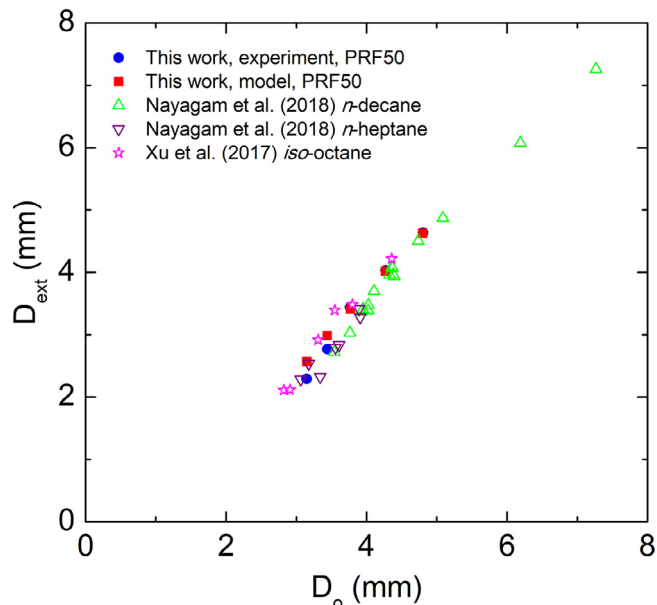


Fig. 6. Variation of radiative extinction diameter with initial droplet diameter for 50/50 *n*-heptane/iso-octane droplets. Experimental data for *n*-heptane and *n*-decane are from [42], and iso-octane data are from [29]. Simulations are shown for the mixture examined in this work.

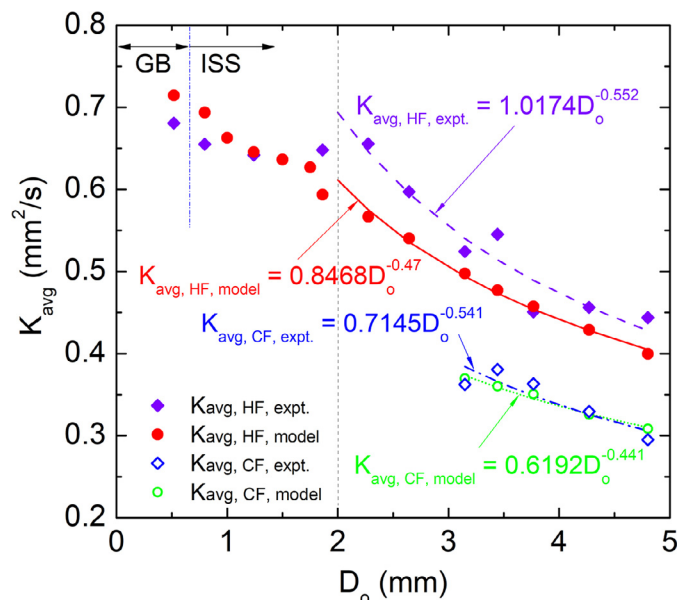


Fig. 7. Dependence of K_{avg} on D_0 , where the correlation equation is valid for $D_0 > 2$ mm. Experimental data for 0.52 mm are from [18].

in Fig. 6 for both simulated and measured mixture and pure component radiative extinction diameters.

The variation of average burning rate (K_{avg}) with D_0 is shown in Fig. 7. Average burn rates from experiments were obtained by linearizing the scaled evolution of droplet diameters in Fig. 5 from scaled time 0.2 s/mm 2 to the end of the HF burning regime. This operation ensured using the most linear portion of the D^2 data by eliminating the initial transient processes. The blue circles in Fig. 5 mark the end of the range of data used in the CF burning regime to obtain an average CF burn rate. Also shown in Fig. 5 are quantitative predictions from the DNM outlined in Section 3. For the numerical data, the average burning rates were obtained by time-averaging the data between 10% - 90% of the total hot flame

and the total cool flame burn time. The initial and final 10% of the burn times were excluded in the time averaging to avoid initial and final transients of the burn process.

The predicted average burning rates in Fig. 7 for both the hot and cool flame mode track well with the measurements, which encompass a wider range of D_o values from where radiation is not important ($D_o < 1$ mm) to where it is important ($D_o > 2$ mm). For the CF regime, the measurements and the predictions almost overlap. However, for the HF mode the predicted average burning rates are lower than the measurements. Similar to the CF burn, the HF burn during the two-stage combustion process is transient as shown in Fig. 5. The HF burn for the large droplets also does not reach a quasi-steady behavior, and the burn rate is time-dependent throughout. So even though time averaging is performed using data in the 10% – 90% range for the HF burn, there is significant temporal variation during that period. The differences of predicted and measured burning rates likely arise from experimental aberrations induced by the ignition event and the fact that the burn rate is based on differentiating the data, which can magnify uncertainties depending on the noise of the data.

It is clear from Fig. 7 that droplets burn slower as D_o increases. However, it appears that K has different levels of dependence on D_o . For submillimeter sized droplets within the limited range, K decreases linearly with D_o . In the submillimeter range, the droplets are exposed to diffusive losses only. For D_o ranging between 1 mm and 2 mm, K is weakly dependent on D_o . In this range, radiative losses are not completely negligible but do have small contributions [43]. Additionally, in this region, diffusive losses are also present. As the mode of loss changes, a small dip in K is observed. However, in between 1.0 mm – 1.75 mm, K has a weak dependence on D_o . For $D_o > 2.0$ mm, radiative losses dominate, and the rate of decrease of burning rate as a function of D_o increases significantly. Both the model and experiments capture the entire trend of the dependence of K on D_o . The prediction only deviates in delineating the limit of the weak dependence. The predictions show that the weak dependence persists till $D_o \sim 1.75$ mm, whereas the experimental limit is $D_o \sim 2.00$ mm.

It was previously shown that when non-luminous radiation is the dominant energy loss mechanism from the flame of a single component droplet, $K \sim D_o^{-n}$ [9]. Both the HF and CF average burning rate data are consistent with this scaling as seen in Fig. 7. For $D_o > 2.0$ mm, this scaling predicts the burning rate for the PRF mixture reasonably well. The simulated and measured data have a similar ‘‘exponent’’ dependence: -0.47 versus -0.55 . It is interesting to note that even though the scaling law was derived for a single component droplet, it applies to the *n*-heptane/isooctane mixture.

For the CF regime which is present for $D_o > 3.0$ mm, the average burning rate has a similar ‘‘power law’’ dependence – an exponent dependence of -0.44 for simulations and -0.54 for experiments. The radiative loss in the CF burn is minimal but is still present to some extent (cf, Fig. 3). The measured average cool flame burning rates do have some scatter, which could be due to the short duration CF as well as a convective effect resulting from droplet drift.

The trends in Fig. 7, which show K decreasing with increasing D_o for the PRF50 system, are different from the trends in pure alkane CF burn rates reported in [44] with increasing D_o . These differences could be indicative of CF burning not being quasi-steady in this study because of the presence of iso-octane in the droplet. The CFs observed here have an extremely small temporal duration. This is the main reason why a decrease in the average burning rate is observed in both experiments and model predictions. In prior work [9,31], alkane droplets underwent long-duration cool flame burns whereby the burning rate temporally increased, reached a peak plateau, and progressively decreased.

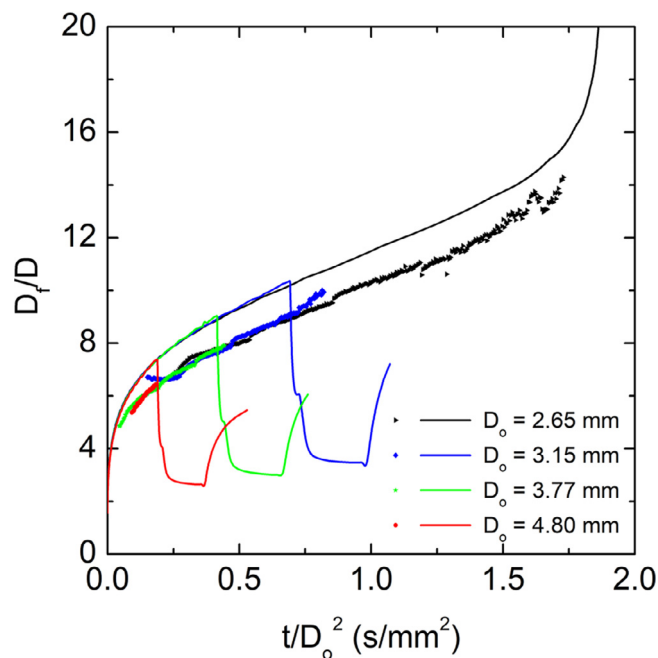


Fig. 8. Evolution of flame standoff ratios for selected 50/50 *n*-heptane/isooctane runs. Symbols and lines represent experimental measurements and numerical predictions, respectively. (For interpretation of the references to color in this figure, the reader is referred to the web version of this article.)

The average CF burning rate under those conditions has a very weak dependence on the initial droplet diameter.

Figure 8 shows the evolution of the relative position of the flame to the droplet surface, $FSR = D_f/D$, for selected D_o for the 50/50 mixture. The simulated FSRs are in reasonable agreement with the measurements, though they are larger. Differences could be due to the accuracy of the D_f measurements since the flame boundary is not as sharp as the droplet boundary, uncertainties in the kinetic mechanism and property inputs for the DNM, or that the simulations do not include soot formation as noted previously.

For $D_o = 2.65$ mm, the flame progressively moves away from the droplet. Radiation losses from the flame were not sufficient to initiate a radiative extinction transition to CF burning. This is consistent with the numerical predictions shown in Fig. 5. For this droplet, the FSR increased throughout burning.

For larger D_o , the FSR measurements were limited by the ability to view the flame structure in the color video, which is difficult when burning enters a CF regime. A time is reached where it is not possible to make any flame diameter measurements. Thereafter, the burn rate decreases as noted previously (Fig. 5), and the DNM predicts an abrupt reduction of the FSR. A flame still, though, exists as predicted by the DNM shown in Fig. 8.

In the CF regime, the simulations show that the FSR and the flame temperatures are almost constant (Fig. 3b) at a much lower value than in the earlier HF region as noted previously. Burning could not be considered fully ‘‘quasi-steady’’ here because burn rates in the CF regime shown in Fig. 5 are not constant due to the time-dependency of the burn rate (the data were nonetheless linearized to give the average burning rates in Fig. 7). Recent work using an averaging technique from UV images taken from similar tests performed with *n*-decane suggests an FSR of approximately 3 for the CF burning regime [44], which is remarkably consistent with the data shown in Fig. 8 (note the flat portions).

As evaporation continues in the CF regime, the flame temperature decreases (Fig. 3b) due to diffusive losses. CF extinction, however, is strongly dictated by low temperature kinetics [45] and in

general coincides with the ketohydroperoxide buildup during the later stage of the burn and decreases in degenerate chain branching from a lack of further reaction. As shown in Fig. 5, the CF extinguishes (note the blue circles) while the FSR begins to rise (Fig. 8) until the non-visible flame would extinguish entirely. The evaporation rate then approaches that of a droplet in a time-varying hot gas as heat diffuses to the surrounding after the CF extinguishes.

5. Conclusions

The burning characteristics of *n*-heptane and iso-octane mixture droplets were examined in experiments carried out on the International Space Station to promote spherical droplet flames and a one-dimensional transport for initial droplet diameters ranging from 0.8 mm to 5 mm. The droplets were free-floating. The data obtained were used to validate a detailed numerical model of the burning process including the kinetic mechanism employed in the simulations. The range of initial droplet diameters examined was large enough to transition burning from a traditional hot flame to cool flame or low temperature combustion, while also including mixture effects in the process.

The numerical simulations were successful in their ability to predict burn rates in both hot and cool flame conditions. Predicted and measured radiative extinction diameters showed a linear relationship that is consistent with prior work on single component systems. Moreover, the evolution of droplet and flame diameters, and the transition to cool flame burning were in good agreement with the simulations. The burning histories showed that the average burn rates decreased as D_o was increased and that for $D_o > 2$ mm the trend followed a power-law relationship in the form $K_{avg} \sim D_o^{-n}$ for both the hot flame and cool flame regimes of burning, which was consistent with a scaling analysis. Droplets with $D_o > 3$ mm radiatively extinguished and burning rates abruptly decreased as burning transitioned to cool flame behavior. No preferential vaporization effect was found owing to the close boiling points of *n*-heptane and iso-octane. The FSR increased with time during burning prior to radiative extinction, and no strong dependence of FSR on D_o in the hot flame burning regime was observed both in the experiments and the simulations.

Declaration of Competing Interest

The authors declare that they have no known competing financial interests or personal relationships that could have appeared to influence the work reported in this paper.

Acknowledgments

This research was supported in part by NASA grants NNX08AI51G and #80NSSC18K0480 (CTA, YX), and NNX14AG461A (TF). The authors thank Dr. Yu-Cheng Liu of Tsinghua University for his interest in our work, Dr. Anthony Reeves and Mr. Yiren Shen of Cornell University for processing some of the video images, and Dr. Frederick Dryer of Princeton University for reading the manuscript and offering some comments.

Supplementary materials

Supplementary material associated with this article can be found, in the online version, at doi:10.1016/j.combustflame.2020.06.012.

References

- [1] H.J. Curran, W.J. Pitz, C.K. Westbrook, G.V. Callahan, F.L. Dryer, Oxidation of automotive primary reference fuels at elevated pressures, *Symp. (Int.) Combust.* 27 (1998) 379–387.
- [2] P.A. Glaude, V. Conraud, R. Fournet, F. Battin-Leclerc, G.M. Côme, G. Scacchi, P. Dagaut, M. Cathonnet, Modeling the oxidation of mixtures of primary reference automobile fuels, *Energy Fuels* 16 (2002) 1186–1195.
- [3] Y. Ra, R.D. Reitz, A combustion model for IC engine combustion simulations with multi-component fuels, *Combust. Flame* 158 (2011) 69–90.
- [4] T.I. Farouk, Y. Xu, C.T. Avedisian, F.L. Dryer, Combustion characteristics of primary reference fuel (PRF) droplets: single stage high temperature combustion to multistage “Cool Flame” behavior, *Proc. Combust. Inst.* 36 (2017) 2585–2594.
- [5] A. Stagni, A. Cuoci, A. Frassoldati, E. Ranzi, T. Faravelli, Numerical investigation of soot formation from microgravity droplet combustion using heterogeneous chemistry, *Combust. Flame* 189 (2018) 393–406.
- [6] S. Kumagai, T. Sakai, S. Okajima, Combustion of free fuel droplets in a freely falling chamber, *Symp. (Int.) Combust.* 13 (1971) 779–785.
- [7] G.S. Jackson, C.T. Avedisian, J.C. Yang, Observations of soot during droplet combustion at low gravity: heptane and heptane/monochloroalkane mixtures, *Int. J. Heat Mass Transf.* 35 (1992) 2017–2033.
- [8] H. Hara, S. Kumagai, The effect of initial diameter on free droplet combustion with spherical flame, *Symp. (Int.) Combust.* 25 (1994) 423–430.
- [9] Y.C. Liu, Y. Xu, M.C. Hicks, C.T. Avedisian, Comprehensive study of initial diameter effects and other observations on convection-free droplet combustion in the standard atmosphere for *n*-heptane, *n*-octane, and *n*-decane, *Combust. Flame* 171 (2016) 27–41.
- [10] A.J. Marchese, F.L. Dryer, R.O. Colantonio, Radiative effects in space-based methanol/water droplet combustion experiments, *Symp. (Int.) Combust.* 27 (1998) 2627–2634.
- [11] K.-O. Lee, S.L. Manzello, M.Y. Choi, The effects of initial diameter on sooting and burning behavior of isolated droplets under microgravity conditions, *Combust. Sci. Technol.* 132 (1998) 139–156.
- [12] S.L. Manzello, M.Y. Choi, A. Kazakov, F.L. Dryer, R. Dobashi, T. Hirano, The burning of large *n*-heptane droplets in microgravity, *Proc. Combust. Inst.* 28 (2000) 1079–1086.
- [13] G. Xu, M. Ikegami, S. Honma, K. Ikeda, X. Ma, H. Nagaishi, D.L. Dietrich, P.M. Struk, Inverse influence of initial diameter on droplet burning rate in cold and hot ambiances: a thermal action of flame in balance with heat loss, *Int. J. Heat Mass Transf.* 46 (2003) 1155–1169.
- [14] G. Xu, M. Ikegami, S. Honma, K. Ikeda, D.L. Dietrich, P.M. Struk, Interactive influences of convective flow and initial droplet diameter on isolated droplet burning rate, *Int. J. Heat Mass Transf.* 47 (2004) 2029–2035.
- [15] A.J. Marchese, F.L. Dryer, V. Nayagam, Numerical modeling of isolated *n*-alkane droplet flames: initial comparisons with ground and space-based microgravity experiments, *Combust. Flame* 116 (1999) 432–459.
- [16] S. Nakaya, K. Fujishima, M. Tsue, M. Kono, D. Segawa, Effects of droplet diameter on instantaneous burning rate of isolated fuel droplets in argon-rich or carbon dioxide-rich ambiances under microgravity, *Proc. Combust. Inst.* 34 (2013) 1601–1608.
- [17] W.M. Haynes, *CRC Handbook of Chemistry & Physics*, 95th ed, Taylor and Francis, an imprint of CRC Press, Boca Raton, Florida, 2014–2015.
- [18] Y.C. Liu, C.T. Avedisian, A comparison of the spherical flame characteristics of sub-millimeter droplets of binary mixtures of *n*-heptane/iso-octane and *n*-heptane/toluene with a commercial unleaded gasoline, *Combust. Flame* 159 (2012) 770–783.
- [19] S. Tanaka, F. Ayala, J.C. Keck, J.B. Heywood, Two-stage ignition in HCCI combustion and HCCI control by fuels and additives, *Combust. Flame* 132 (2003) 219–239.
- [20] A workshop to identify research needs and impacts in predictive simulation for internal combustion engines (PreSICE), 2011. http://www1.eere.energy.gov/vehiclesandfuels/pdfs/presice_rpt.pdf (Accessed September 21, 2014).
- [21] T. Kadota, S. Mizutani, C.-Y. Wu, M. Hoshino, Fuel droplet size measurements in the combustion chamber of a motored SI engine via laser mie scattering, 1990, SAE Technical Paper 900477.
- [22] M. Tabata, A. Nagao, Y. Iida, Studies of fuel droplets behavior and flame propagation in combustion chamber on S.I. engine using laser 2-D visualization, *International Symposium COMODIA*, 90 (1990), pp. 179–184.
- [23] M.M. Maricq, D.H. Podsiadlik, D.D. Brehob, M. Haghgooei, Particulate emissions from a direct-injection spark-ignition (DISI) engine, 1999, SAE Technical Paper 1999-01-1530.
- [24] F. Zhao, M.C. Lai, D.L. Harrington, Automotive spark-ignited direct-injection gasoline engines, *Progr. Energy Combust. Sci.* 25 (1999) 437–562.
- [25] D.L. Dietrich, V. Nayagam, M.C. Hicks, P.V. Ferkul, F.L. Dryer, T. Farouk, B.D. Shaw, H.K. Suh, M.Y. Choi, Y.C. Liu, C.T. Avedisian, F.A. Williams, Droplet combustion experiments aboard the international space station, *Microgravity Sci. Technol.* 26 (2014) 65–76.
- [26] B. Banu, Fluids and combustion facility (FCF) and combustion integrated rack (CIR), NASA John H. Glenn Research Center, 2008 Payload Accommodations Handbook CIR-DOC-4064.
- [27] J. Robbins, C. Shinn, Multi-user droplet combustion apparatus flex2, NASA John H. Glenn Research Center, 2010 Reflight Safety Data Package MDC-DOC-1790A.
- [28] C.L. Dembia, Y.C. Liu, C.T. Avedisian, Automated data analysis for consecutive images from droplet combustion experiments, *Image Anal. Stereol.* 31 (2012) 137–148.
- [29] Y. Xu, M.C. Hicks, C.T. Avedisian, The combustion of iso-octane droplets with initial diameters from 0.5 to 5 mm: effects on burning rate and flame extinction, *Proc. Combust. Inst.* 36 (2017) 2541–2548.

- [30] T.I. Farouk, M.C. Hicks, F.L. Dryer, Multistage oscillatory “Cool Flame” behavior for isolated alkane droplet combustion in elevated pressure microgravity condition, *Proc. Combust. Inst.* 35 (2015) 1701–1708.
- [31] T.I. Farouk, F.L. Dryer, Isolated n-heptane droplet combustion in microgravity: “Cool Flames” – two-stage combustion, *Combust. Flame* 161 (2014) 565–581.
- [32] F.E. Alam, Y.C. Liu, C.T. Avedisian, F.L. Dryer, T.I. Farouk, n-Butanol droplet combustion: numerical modeling and reduced gravity experiments, *Proc. Combust. Inst.* 35 (2015) 1693–1700.
- [33] F.E. Alam, S.H. Won, F.L. Dryer, T.I. Farouk, Ozone assisted cool flame combustion of sub-millimeter sized n-alkane droplets at atmospheric and higher pressure, *Combust. Flame* 195 (2018) 220–231.
- [34] M. Mehl, W.J. Pitz, C.K. Westbrook, H.J. Curran, Kinetic modeling of gasoline surrogate components and mixtures under engine conditions, *Proc. Combust. Inst.* 33 (2011) 193–200.
- [35] A. Raj, I.D.C. Prada, A.A. Amer, S.H. Chung, A reaction mechanism for gasoline surrogate fuels for large polycyclic aromatic hydrocarbons, *Combust. Flame* 159 (2012) 500–515.
- [36] T.E. Daubert, R.P. Danner, Physical and thermodynamic properties of pure chemicals: data compilation, Hemisphere Publishing, New York, 1989.
- [37] G.S. Jackson, C.T. Avedisian, Modeling of spherically symmetric droplet flames including complex chemistry: effect of water addition on n-heptane droplet combustion, *Combust. Sci. Technol.* 115 (1996) 125–149.
- [38] T.I. Farouk, Y.C. Liu, A.J. Savas, C.T. Avedisian, F.L. Dryer, Sub-millimeter sized methyl butanoate droplet combustion: microgravity experiments and detailed numerical modeling, *Proc. Combust. Inst.* 34 (2013) 1609–1616.
- [39] C.J. Mueller, G.C. Martin, Effects of oxygenated compounds on combustion and soot evolution in a DI diesel engine: broadband natural luminosity imaging, 2002, SAE Technical Paper 2002-01-1631.
- [40] R.A. Dobbins, Soot inception temperature and the carbonization rate of precursor particles, *Combust. Flame* 130 (2002) 204–214.
- [41] M.C. Hicks, V. Nayagam, F.A. Williams, Methanol droplet extinction in carbon-dioxide-enriched environments in microgravity, *Combust. Flame* 157 (2010) 1439–1445.
- [42] V. Nayagam, D.L. Dietrich, M.C. Hicks, F.A. Williams, Radiative extinction of large n-alkane droplets in oxygen-inert mixtures in microgravity, *Combust. Flame* 194 (2018) 107–114.
- [43] T.I. Farouk, F.L. Dryer, On the extinction characteristics of alcohol droplet combustion under microgravity conditions – a numerical study, *Combust. Flame* 159 (2012) 3208–3223.
- [44] V. Nayagam, D.L. Dietrich, F.A. Williams, Partial-burning regime for quasi-steady droplet combustion supported by cool flames, *AIAA J.* 54 (2016) 1235–1239.
- [45] K. Seshadri, N. Peters, F.A. Williams, V. Nayagam, G. Paczko, Asymptotic analysis of quasi-steady n-heptane droplet combustion supported by cool-flame chemistry, *Combust. Theory Model.* 20 (2016) 1118–1130.